Synthesis, Characterization, and Electrochemical Properties of Reduced Graphene Oxide Produced from Sugarcane Bagasse for Supercapacitor Applications

Ikhwan Darmawan [1] ⓘD , Likkhasit Wannasen [1,2] ⓘD , Supree Pinitsoontorn [1,2,*] ⓘD

[1]   Material Science and Nanotechnology Program, Department of Physics, Faculty of Science, Khon Kaen University, Khon Kaen, Thailand
[2]   Institute of Nanomaterials Research and Innovation for Energy (IN-RIE), Khon Kaen University, Khon Kaen 40002, Thailand
*   Correspondence: psupree@kku.ac.th;

Abstract: Reduced graphene oxide (RGO) stands out as a highly promising material with numerous potential applications. Various carbon sources can be used as starting materials for the production of RGO. This study explores the utilization of sugarcane bagasse (SB), a globally abundant agricultural waste material, as a precursor for RGO synthesis. Initially, SB underwent pyrolysis at 750°C at the rate of 10°C/min under flowing argon gas to extract the graphite phase. The Hummer's method was then employed to convert the extracted graphite into graphene oxide (GO). The GO products were subjected to ultrasonication to break oxygen functional groups before reduction into RGO, using metallic zinc (Zn) as a reducing agent. The graphitic transformation at each synthesis step, from graphite to GO and, ultimately, to RGO, was confirmed through XRD and FTIR analyses. Additionally, the formation of RGO was further confirmed by Raman spectroscopy, which showed the characteristic D, G, and 2D bands of the RGO phase. SEM micrographs revealed the morphology of RGO as a flake-like 2D multilayer nanosheet with a sheet thickness of several hundred nm. This study also examines the effect of Zn powder concentration on GO reduction to form RGO. It was found that the appropriate amount of Zn was crucial for RGO synthesis, as an excessive amount led to the presence of Zn residue in RGO samples. These findings present a straightforward and effective approach to preparing RGO from sugarcane bagasse, which can be scaled up for industrial production. Furthermore, the investigation into the electrochemical properties of the RGO samples revealed excellent performance under optimized synthesis conditions, including a large surface area, high specific capacitance, conductivity, and good stability. This positions the RGO samples produced from SB as a promising electrode material for supercapacitor applications.

Keywords: RGO; Hummer's method; carbon electrode; sugarcane bagasse; supercapacitor.

1. Introduction

Graphene is a highly promising material with unique properties since its discovery in 2004 [1,2]. Its thin, 2D hexagonal structure, composed of sp^2-bonded carbon atoms in a monolayer planar sheet, presents intriguing possibilities for technological advancements [3]. Graphene and its derivatives hold the potential to revolutionize many next-generation technologies, including high-frequency electronics, gas sensors, broadband photodetectors, and transparent conductive coatings [4,5]. In particular, one notable derivative, reduced graphene

oxide (RGO), has demonstrated its utility in various fields, such as thermoelectric applications [6], skeletal implants [7], water purification [8], electrical components, and other uses [9–11].

The reduced graphene oxide (RGO) synthesis from graphite has proven successful through various methods, encompassing mechanical and chemical processes [12]. Among the chemical routes, the Hummer method is the most promising technique for large-scale graphene production [13]. Originally introduced by Hummers and Offerman in 1958, this method involves the oxidation of flake graphite using $NaNO_3$, H_2SO_4, and $KMnO_4$ to synthesize graphene oxide (GO) [14]. Ultrasonication is employed to break down the oxygen functional groups in GO [15,16] to convert GO into RGO. Zn powder is added as a reducing agent. Zn in the acid solution is converted to Zn^{2+} [17], and then the resulting oxygen oxidizes Zn^0 to become Zn^{2+} in the form of ZnO and $Zn(OH)_2$ [18,19]. Consequently, GO is reduced, and RGO is produced [20].

There are various potential sources of carbon for the production of RGO. Several parts of plants, such as leaves, fruits, flowers, bark, seeds, roots, and stems, have been demonstrated as suitable starting materials for RGO production [21]. Cinnamon bark has successfully produced RGO using a reflux approach [22]. Mango leaves have proven to be an effective raw material for producing RGO through chemical reaction routes [23]. The Hummer's method has also been utilized to produce RGO from Damask Rose flowers [24]. These examples highlight the potential for RGO production from agricultural waste materials. In this study, we have chosen sugarcane bagasse as the raw material.

Sugarcane bagasse (SB) is an abundant agricultural waste material found worldwide. It primarily consists of cellulose fiber and is easily convertible at low temperatures, making it an ideal precursor material. Using Hummer's reagent, we can oxidize the graphite present in SB, producing graphene oxide (GO). An effective method for reducing GO is to utilize Zn Powder, which has been demonstrated to react with oxygen and form ZnO in an acidic solution [25]. The introduction of Zn as a reducing agent during the treatment of GO leads to the subsequent production of RGO.

Consequently, our study provides a comprehensive analysis of the effects of varying Zn mass on the microstructure and morphology of the resultant RGO. Additionally, RGO is one of the carbon derivations proven to exhibit stable performance for supercapacitors [26]. Therefore, the RGO produced from SB in this work is subjected to electrochemical properties study as a potential electrode material for supercapacitor applications.

2. Materials and Methods

The general steps for producing RGO from graphite are summarized in Figure 1. The process begins with the exfoliation of graphite in an acid solution. Next, the graphite nanosheets undergo oxidation using an oxidizing agent to obtain GO. Subsequently, ultrasonication is applied to break oxygen functional groups within the GO structure. Finally, adding Zn facilitates the reduction process, resulting in the formation of RGO [20]. In our research, SB was used as an initial source for graphite. The detailed process is explained below.
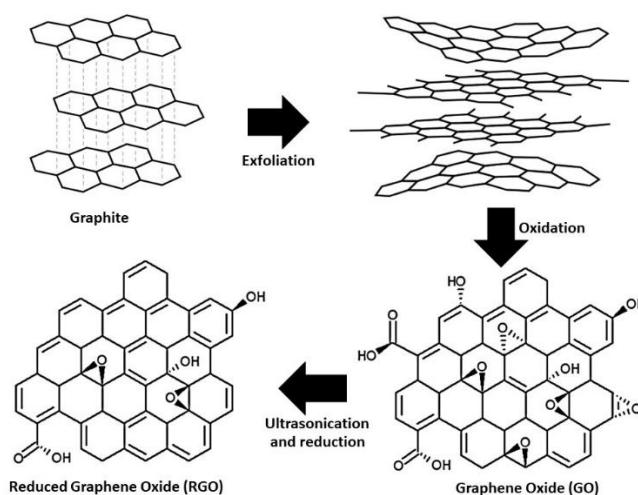
Figure 1. A schematic illustration of the process for producing RGO from graphite.

2.1. Production of graphite from Sugarcane Bagasse (SB).

Graphite was produced from sugarcane bagasse (SB), an agricultural waste product. The SB was first dried and then mechanically mashed using a homogenizer (JGY-800B, Yongkang Hardware Capital, Zhejiang, China). The mashed SB was sieved through a stainless-steel sieve, resulting in a particle size of less than 125 µm of SB powder. The SB powder was then subjected to pyrolysis at 750°C in a quartz-tube furnace under an Ar atmosphere for 2 hours, with Ar gas flowing continuously throughout the pyrolysis process at a rate of 10°C/minute. The yield of graphite produced from pyrolysis is 21.35% by weight. A schematic diagram of this process is depicted in Figure 2.
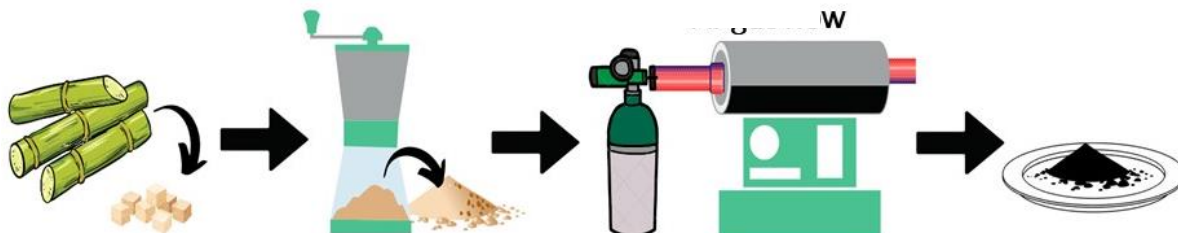

Figure 2. A schematic illustration of the process for producing graphite from sugar bagasse (SB).

2.2. Preparation of graphene oxide (GO).

The preparation of GO was conducted using Hummer's method. Initially, 2 g of graphite from sugarcane bagasse (GSB) was placed into a beaker, and 98 mL of H_2SO_4 (M_w= 98.08, RCI Labscan, 98%) was added. Subsequently, 4 g of $NaNO_3$ (M_w= 84.99, Sigma-Aldrich, 99.5%) was introduced, and the mixture was stirred for an hour. The reaction was then maintained at approximately 5°C by placing the beaker in a container filled with ice cubes, while 8 g of $KMnO_4$ (M_w= 158.03, Sigma-Aldrich, 99%) was gradually added. After 24 hours of stirring, black-colored precipitates were formed. At this stage, 100 mL of water and 20 mL of H_2O_2 (30%) (M_w= 34.01, Sigma-Aldrich, 30%) were gradually added and stirred for 30 minutes. The resulting mixture was centrifuged at 2500 rpm for 2.5 hours to precipitate the sample. Subsequently, 80 mL of 0.01M HCl (M_w= 36.46, RCI Labscan, 35%) was added to the sample and then washed with deionized water until achieving a pH of 7. Finally, the sample was dried in an oven. A schematic illustration of the process is shown in Figure 3.
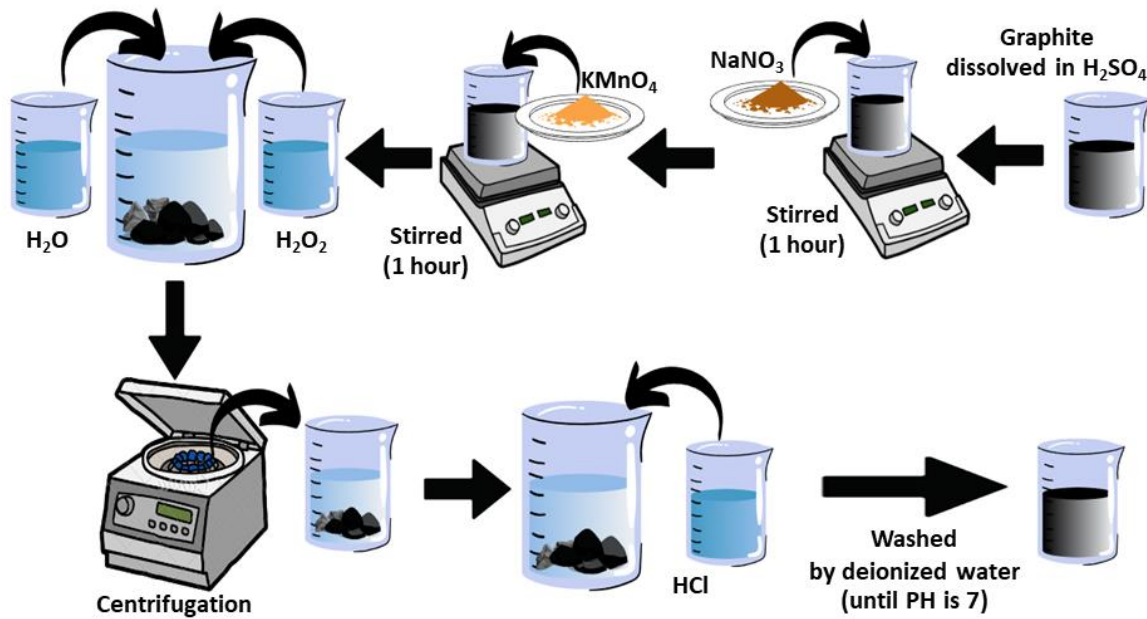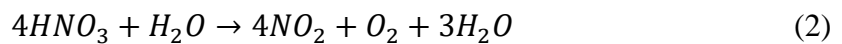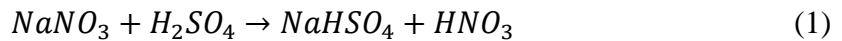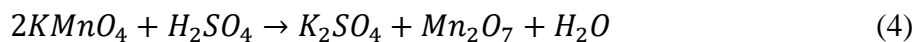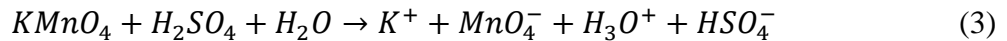
Figure 3. A schematic illustration of the process for producing graphene oxide (GO).
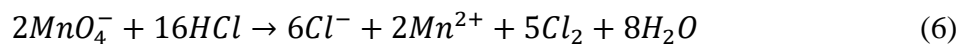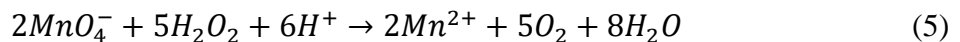
In our process, the production of GO from GSB involves the use of H_2SO_4 and $NaNO_3$ to initiate oxidation, as described by the following reactions [27]:

$$NaNO_3 + H_2SO_4 \rightarrow NaHSO_4 + HNO_3 \tag{1}$$
$$4HNO_3 + H_2O \rightarrow 4NO_2 + O_2 + 3H_2O \tag{2}$$

Graphite undergoes oxidation at the edge sites, leading to intercalation between the layers of graphite [27]. The addition of $KMnO_4$ enhances the oxidation rate, as the oxidizing agent is generated through the following reactions:

$$KMnO_4 + H_2SO_4 + H_2O \rightarrow K^+ + MnO_4^- + H_3O^+ + HSO_4^- \tag{3}$$

$$2KMnO_4 + H_2SO_4 \rightarrow K_2SO_4 + Mn_2O_7 + H_2O \tag{4}$$

The oxidation reaction is stopped by adding H_2O_2 and HCl, producing Mn^{2+}, O_2, Cl_2, and H_2O, according to the reactions below. The reaction products are then easily removed by water.

$$2MnO_4^- + 5H_2O_2 + 6H^+ \rightarrow 2Mn^{2+} + 5O_2 + 8H_2O \tag{5}$$

$$2MnO_4^- + 16HCl \rightarrow 6Cl^- + 2Mn^{2+} + 5Cl_2 + 8H_2O \tag{6}$$

2.3. Synthesis of reduced graphene oxide (RGO).

To synthesize RGO, the process began with ultrasonication of GO from the previous procedure using a 40 kHz ultrasonic cleaner (GT Sonic-D9, China) for an hour. Zn powder (M_w= 65.38, Kemaus, 99.5%) was then added as the reducing agent. The reduction of graphene oxide (GO) is achieved through the reaction with Zn, which interacts with oxygen-functional groups as shown below:

$$2Zn + 3OH^- + H_2O \rightarrow Zn(OH)_2 + ZnO + H_3O^+ \tag{7}$$
$$Zn + 2H_3O^+ \rightarrow ZnH_2 + 2H_2O \tag{8}$$
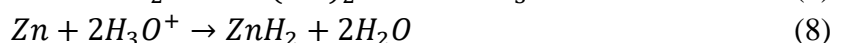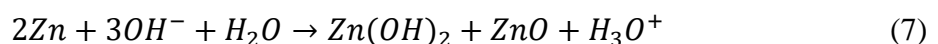
Various amounts of Zn powders were used to investigate the effect of Zn concentration (0.5 g, 2 g, and 4 g). Subsequently, 10 mL of HCl (35%) (M_w= 36.46, RCI Labscan, 35%) was added to remove Zn impurities, followed by thorough washing with deionized water until reaching a pH of 6. The resulting RGO samples were then dried in an oven. Figure 4 summarizes the process for producing RGO from GO. In addition, Table 1 summarizes the sample conditions and their designations.
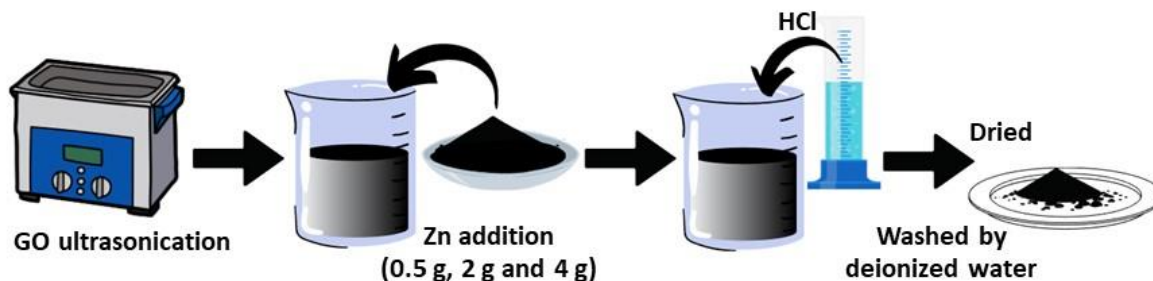

Figure 4. A schematic illustration of the reduced graphene oxide (RGO) process.

Table 1. Sample classifications.

Sample	Zn Addition (g)	Designation
Sugarcane bagasse	-	SB
Graphite from sugarcane bagasse	-	GSB
Graphene oxide	-	GO
Reduced graphene oxide	0.5	RGO-0.5
Reduced graphene oxide	2	RGO-2
Reduced graphene oxide	4	RGO-4

2.4. Characterization.

2.4.1. Microstructure and morphology analysis.

Each sample's phase and crystal structure were analyzed using an X-ray diffraction (XRD) technique (Empyrean, PANalytical, Almelo, Netherland) with Cu K_α radiation. Graphitic phase verification was done using Raman spectroscopy (XploRA plus, Horiba, Kyoto, Japan) with a laser excitation wavelength of 532 nm. The functional groups of the synthesized samples were identified using Fourier transform infrared spectroscopy (FTIR) analysis (TENSOR27, Bruker, Osaka, Japan). The morphology of the samples was studied using a field-emission scanning electron microscope (FE–SEM, Helios Nanolab G3 CX, FEI, Brno, Czech Republic). The specific surface area (SSA) and pore size distribution were analyzed using N_2 adsorption-desorption measurement (Micromeritics, 3Flex, Tokyo, Japan). The PSD was determined by density functional theory (DFT).

2.4.2. Electrochemical performance.

The electrochemical properties of the sample were tested using a three-electrode system, with Ag/AgCl as a reference electrode and platinum as a counter electrode, in a 1 M KOH electrolyte solution. The sample electrode was prepared by mixing 90 wt.% of the sample with 10 wt.% binders, consisting of polyvinylidene fluoride (PVDF) and N-methyl-2-pyrrolidone (NMP) solution at the ratio of 1:20. The mixture was coated on an area of 1×1 cm^2 on a nickel foam substrate (1×1.5 cm^2) before hydraulic pressing at 5 MPa. The galvanostatic charge/discharge (GCD), cyclic voltammetry (CV), electrochemical impedance spectra (EIS), and retention charge/discharge (RCD) were measured using a CORRTEST (CS350

Potentiostat/Galvanostat, Corrtest instruments, Wuhan, China). The specific capacitance can be calculated from GCD by the following equation [26,28]:

$$C_{SP}(F/g) = \frac{I \times \Delta t}{m \times \Delta V} \qquad (9)$$

where I is the current density, Δt is the discharge time, m is the active mass of the sample, and ΔV corresponds to the different potential during discharge.

For the CV measurements, the scan rate was 20 mV s^{-1}, with a voltage range from -1.0 to 0.0. The specific capacitance from the cyclic voltammogram is calculated from the equation below [29]:

$$C_{SP}(F/g) = \frac{\int idV}{2 \times m \times S \times \Delta V} \qquad (10)$$

where $\int idV$ is obtained from the integrated area under the CV curve, and S is the scan rate. Additionally, cyclic stability was measured after 1,000 charge-discharge cycles. The conductivity of electrodes was measured by the EIS method within a frequency range of 0.01 – 10^5.

3. Results and Discussion

3.1. Microstructure and morphology.

3.1.1. XRD.

The XRD patterns of the mashed SB, graphite after pyrolysis of SB (GSB), and graphene oxide (GO) after oxidizing GSB and ultrasonication are shown in Figure 5a. The XRD pattern of SB displays two peaks at 2θ of ~15° and ~22°, corresponding to the cellulose (110) and (200) planes, respectively [30–32]. In contrast, the GSB sample exhibits an XRD pattern with broad humps at 2θ of ~23° and ~43°, the characteristic of amorphous carbon [33]. These 2θ positions are also associated with the (002) and (100) graphitic peaks, consistent with a previous report [34,35]. The XRD results confirm graphite production using SB as the initial source. Subsequently, the GSB underwent further processing to convert it into GO. The XRD pattern of GO in Figure 5a shows more prominent broad humps at ~23° and ~43°, with significantly stronger diffracted intensities compared to GSB.
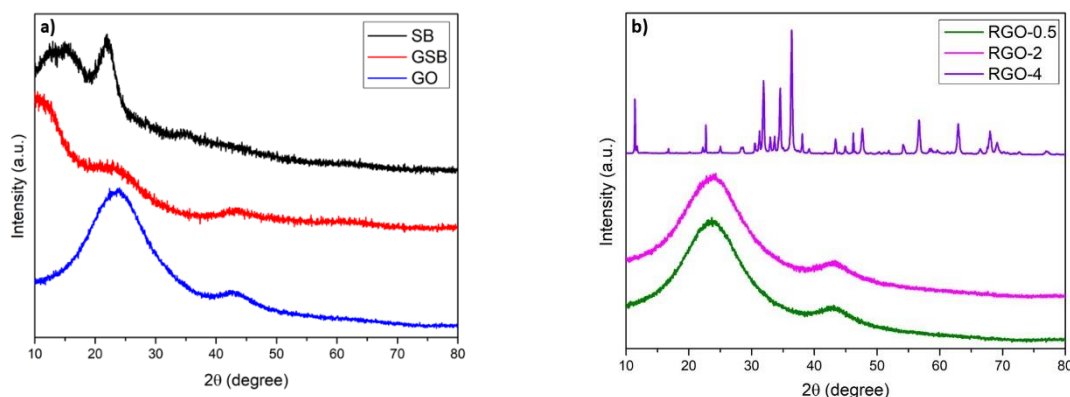

Figure 5. XRD patterns of **(a)** sugarcane bagasse (SB), graphite obtained from sugarcane bagasse (GSB), and graphene oxide (GO); **(b)** reduced graphene oxide (RGO) obtained by adding various masses of Zn to GO (RGO-0.5, RGO-2, and RGO-4).

According to the procedure outlined in Section 2.3, GO was reduced to RGO by the addition of Zn powders. The effect of Zn concentration on the conversion process is illustrated through XRD analysis, as shown in Figure 5b. With a small addition of Zn powders, no

structural changes can be obviously visualized from the XRD patterns, as the patterns for RGO-1 and RGO-2 are very similar. Two broad peaks, indicating some degrees of disorder arrangement of carbon atoms [35], are observed at 2θ around 23° and 43°, corresponding to the (002) and (100) peaks for RGO, as previously reported [36]. However, adding excessive Zn powder (4 g) leads to totally different XRD patterns. Many sharp peaks are observed, likely originating from impurities (Zn, ZnO, $Zn(OH)_2$, and ZnH_2), indicating that overdosing the Zn-reducing agent is not the optimized condition for synthesizing RGO.

3.1.2. FTIR.

Functional groups bonding to the carbon were analyzed by FTIR, as depicted in Figure 6. In the FTIR analysis of GSB, the broad bands appeared at approximately 1061 cm^{-1}, 1550 cm^{-1}, and 2093 cm^{-1}, corresponding to ether (C–O–C), carbon double bond (C=C), and CH_2 stretching. The FTIR spectra show that GO and RGO (RGO-0.5 and RGO-2) exhibit similar patterns, characterized by strong bands at approximately 1100 cm^{-1}, 1563 cm^{-1}, and 1708 cm^{-1}, representing ether functional groups (C–O–C), carbon double bonds (C=C), and carbonyl groups (C=O), respectively [37]. Broad bands at around 2089 cm-1 and 3110 are also observed, corresponding to CH_2 and hydroxyl (OH) groups, respectively [38].

With the addition of 4 g Zn (RGO-4), a strong absorption band of the carbon double bond (C=C) is observed at ~1547 cm^{-1}, slightly shifted from the other samples. Additional bands are presented at ~1708 cm^{-1} and ~2077 cm^{-1}, corresponding to the remaining C=O and CH_2, but the intensities of these bands are significantly reduced. These FTIR results indicate the formation of RGO. However, this sample also displays a strong absorption band at ~693 cm^{-1}, assigned to the presence of zinc oxide (Zn–O). Additionally, the stronger band at approximately ~3434 cm^{-1}, corresponding to OH stretching, suggests the formation of $Zn(OH)_2$.
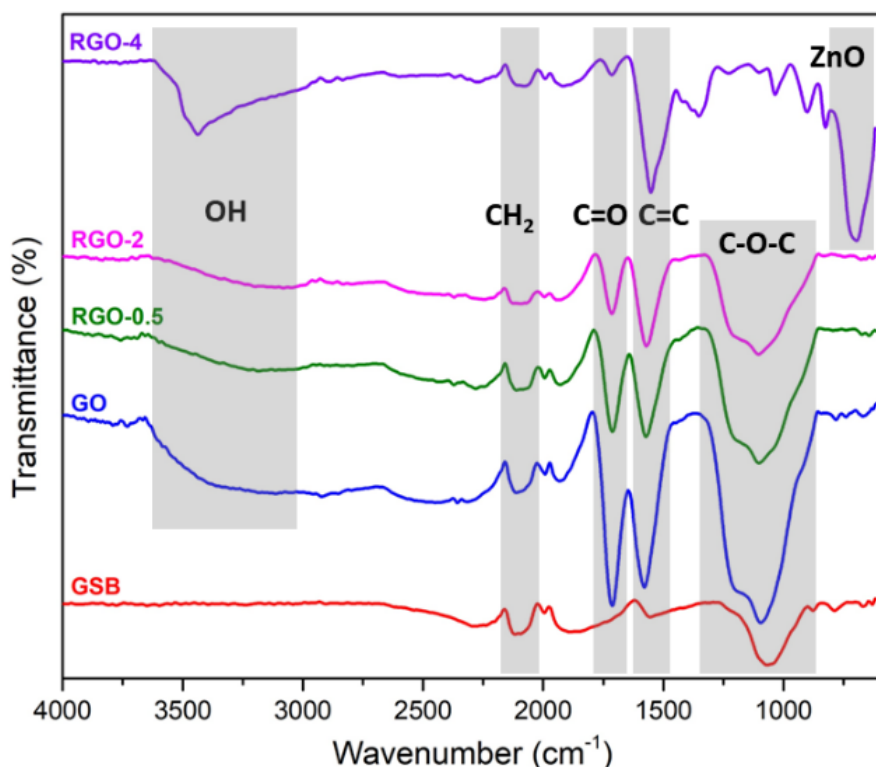

Figure 6. FTIR spectra of RGO.

3.1.3. Raman spectra.

In order to differentiate the class of carbon present in the GO and RGO samples, Raman Spectroscopy was employed to examine the graphitic structure, as shown in Figure 7. The D, G, and 2D bands on the Raman spectrum describe the graphitic information. The D band corresponds to the disorder of carbon atoms, while the G band arises from sp^2-hybridization in the graphitic structure. The 2D band corresponds to the disorder defect of the hexagonal structure of the sp^2 carbon lattice and edge effects of RGO [39–41]. It provides crucial information about the structural and electronic properties of RGO, such as its layer thickness, the presence of multiple layers (e.g., bilayer or multilayer), and the degree of disorder or strain in the lattice [42].
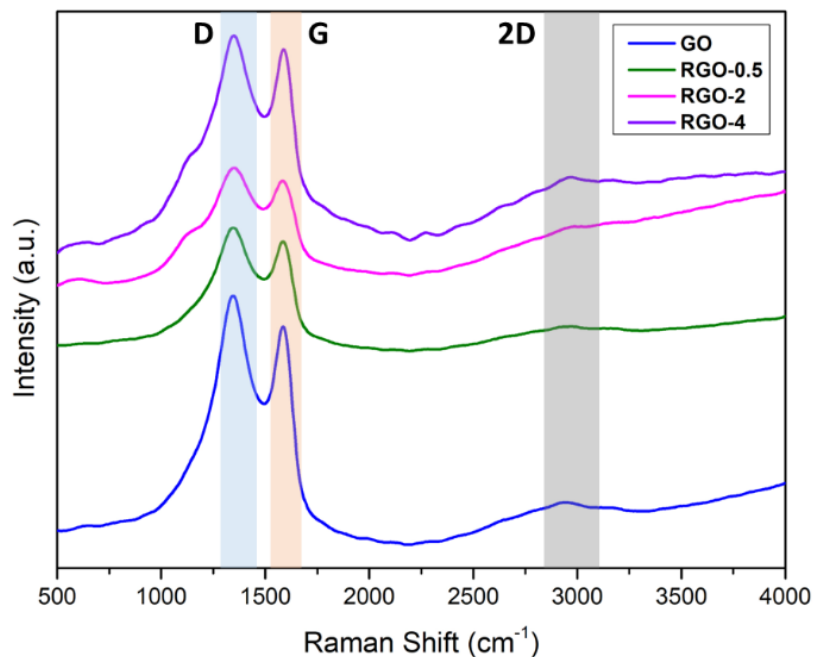

Figure 7. Raman pattern after additional Zn powder.

The positions of the Raman shift for the D, G, and 2D bands, along with the intensity ratio (I_D/I_G) obtained from the spectra, are summarized in Table 2. The D and G band (ID/IG) ratio was affected by adding Zn powder as a reducing agent, ranging from no Zn to 4 g Zn. The intensity ratio (I_D/I_G) is used to evaluate the degree of disorder and defects in the graphitic structure [43]. It was observed that an increase in the amount of Zn led to a decrease in the value of the intensity ratio (I_D/I_G), indicating an increase in the formation of sp^2-hybridization. Another notable feature is the broadening of a region near 2968 cm^{-1} (2D band), which characterizes the layers of RGO (monolayer, double layers, or multilayers). The 2D band corresponds to the multilayer structure of RGO, as monolayer graphene is typically observed at ~2679 cm^{-1} [36].

Table 2. The Raman shift positions for the D, G, and 2D bands and their I_D/I_G ratios.

Sample	Raman shift (cm^{-1})			I_D/I_G
	D	**G**	**2G**	
GO	1342.82	1586.24	2948	1.075
RGO-0.5	1348.84	1592.09	2968	1.071
RGO-2	1345.46	1591.71	2973	1.033
RGO-4	1353.95	1584.63	2953	1.031

3.1.4. Microscopy analysis.

Microscopy analysis using FE-SEM at 10,000 times magnification shows that RGO exhibits a flake-like 2D multilayer nanosheet morphology, as depicted in Figure 8, consistent with Raman analysis. The surface of GSB (Figure 8a) appears rough and becomes smoother after ultrasonication (Figure 8b), indicating the breaking of functional groups [15]. The thickness significantly decreases upon adding 0.5 g Zn, from 713 nm (Fig. 8b) to 383.7 nm (Figure 8c). In contrast, adding 2 g (Figure 8d) and 4 g Zn (Figure 8e) results in thicker layers, measuring 440 nm and 473.9, respectively. The presence of impurities and crystalline structures on the surface of RGO is noticeable with the addition of 4 g Zn, confirming an excess of Zn.
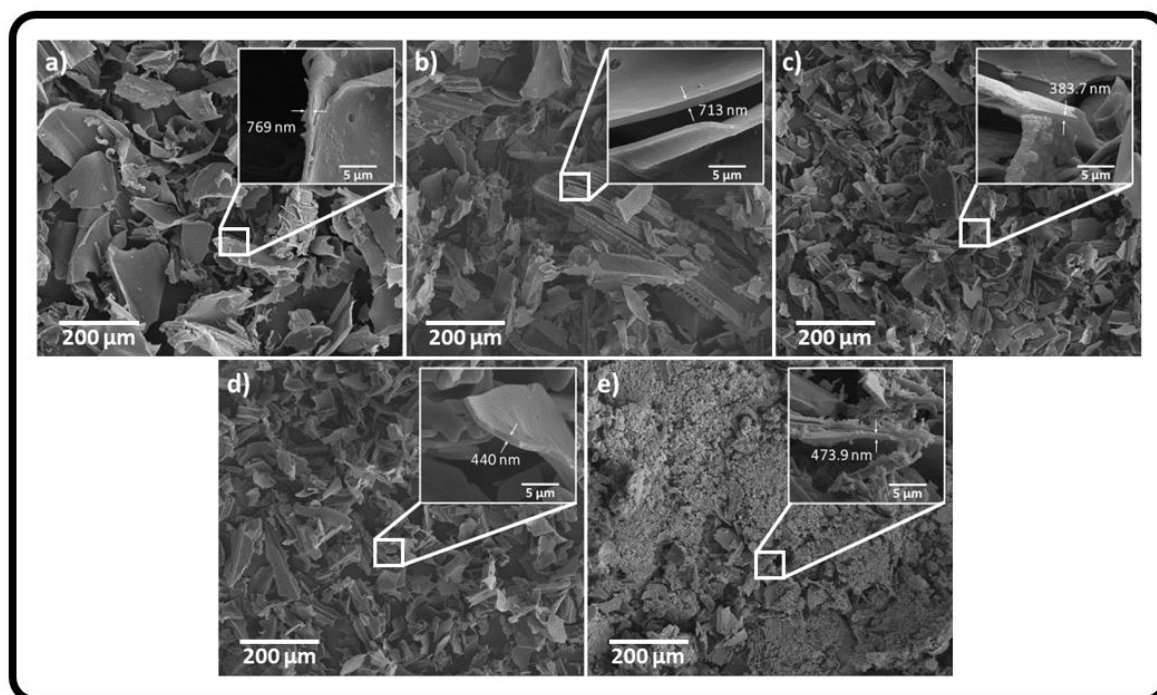

Figure 8. FE-SEM in 10,000 times magnification; **(a)** GSB; **(b)** GO; **(c)** RGO-0.5; **(d)** RGO-2; **(e)** RGO-4.

3.1.5. N_2 adsorption-desorption.

N_2 adsorption-desorption measurements determined the specific surface area (SSA) and pore size distribution. Figure 9 (a) shows the N_2 adsorption-desorption isotherms of each sample. The SSA values of SB, GSB, GO, RGO-0.5, RGO-2, and RGO-4, calculated using the Brunauer–Emmett–Teller (BET) method, are 1.74, 373.98, 435.46, 436.03, 459.53, and 8.45 m^2/g, respectively. The SSA increases from SB to GSB, GO, and RGO. However, with an excessive amount of Zn (4 g) added in the reduction process, the SSA of the RGO-4 suddenly drops. These results are consistent with other characterization techniques (XRD, FTIR, SEM). Figures 9 (b) and 9 (c) plot the micropore and mesopore size distributions. The micropore main peak is at around 0.6-1.3 nm. The micropore and mesopore volumes of RGO-2 are maximized compared to other samples, corresponding to the highest SSA of this sample. Figure 9d summarizes the SSA of all samples for the different pore types. From the BET calculation, it can be seen that micropores mainly contribute to the total SSA.
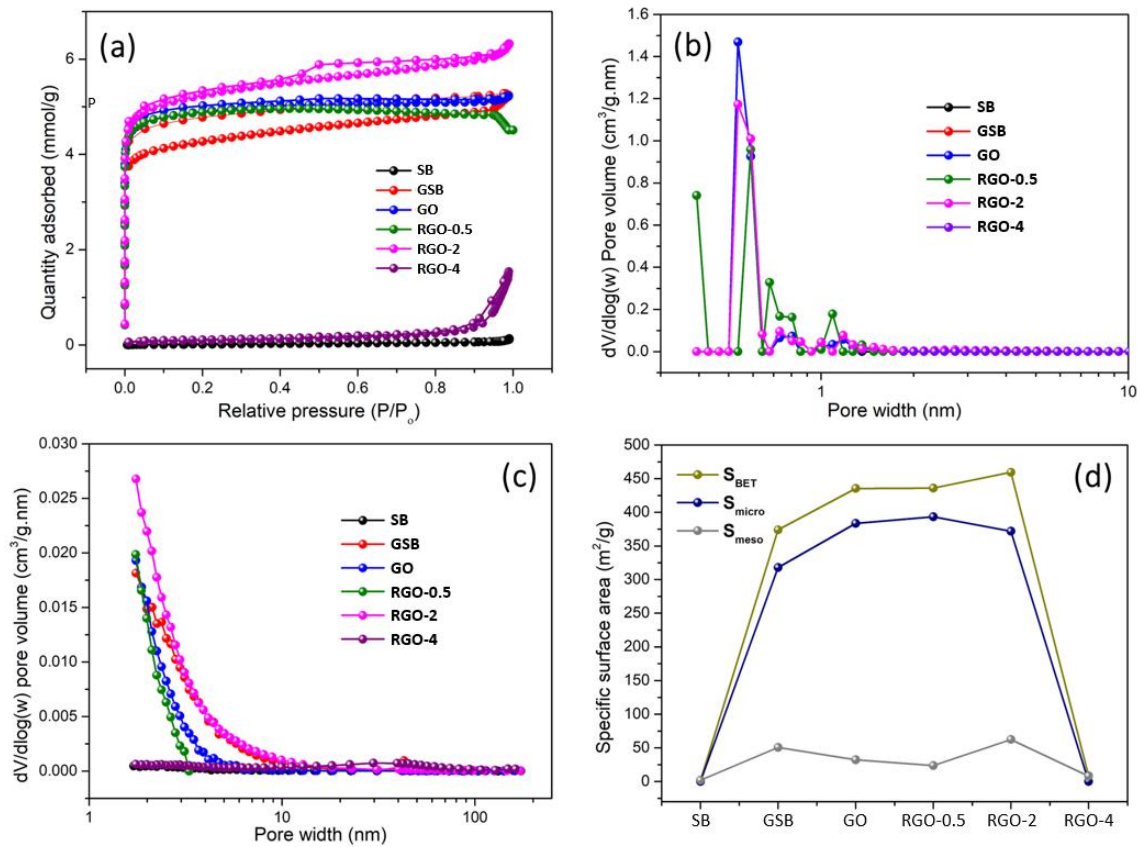
Figure 9. N_2 Adsorption-Desorption; **(a)** isothermal curve; **(b)** micropore distribution; **(c)** mesopore distribution; **(d)** S_{BET}, S_{micro}, and S_{meso} values for every sample.

3.2. Electrochemical properties.

The comparative GCD curves for different samples at a current density of 0.5 A g^{-1} are shown in Figure 10. Each sample exhibits a triangle-like symmetric curve (Figure 10 (a)), confirming favorable characteristics for supercapacitor electrodes. Figure 10 (b) compares the samples' specific capacitance (CSP). The conversion from GSB to GO dramatically increased C_{SP}, rising from 17.78 F g^{-1} to 57.03 F g^{-1}. Furthermore, RGO-2 achieves the highest C_{SP} of 58.38 F g^{-1}, aligning with this sample's superior characteristics of phase, functional groups, morphology, and surface area. In contrast, the RGO-4 sample shows a significant drop in C_{SP} to 6.77 F g^{-1}, attributed to the excessive amount of Zn reducing agent.
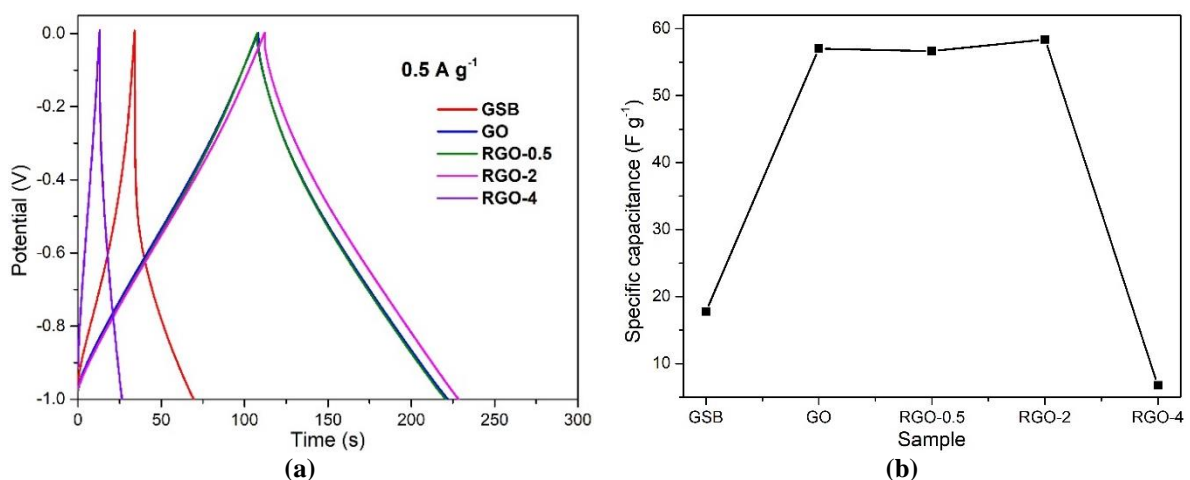

Figure 10. (a) Galvanostatic charge-discharge (GCD); **(b)** Specific capacitance (C_{SP}) from GCD curves.

The cyclic voltammogram (CV) curve is depicted in Figure 11 (a), whereas Figure 11 (b) compares the C_{SP} obtained from the CV curve between samples. The GSB sample exhibits a small loop area, corresponding to its low C_{SP} of 16.06 F g^{-1}. Upon conversion to GO, the CV loop area increases, resulting in an increased C_{SP} of 58.74 F g^{-1}. The C_{SP} further increases upon reduction to RGO-0.5 and RGO-2, with the C_{SP} values of 61.80 F g^{-1} and 65.59 F g^{-1}, respectively. However, the excessive addition of Zn in RGO-4 deteriorates the electrochemical performance, and the C_{SP} significantly reduces to 9.79 F g^{-1}. The electrochemical properties measured using the CV techniques correspond well with the results from GCD measurement.
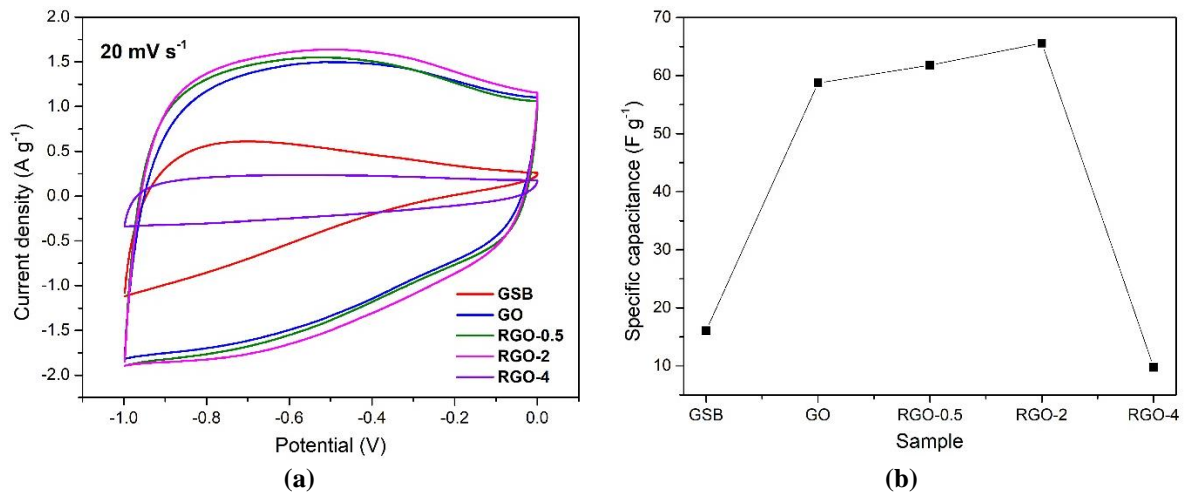

Figure 11. (a) Cyclic voltammogram (CV); **(b)** Specific capacitance (C_{SP}).

The conductivity can be observed in Figure 12 (a) through Nyquist plots, corresponding to charge transfer resistance and equivalent resistance, obtained using the EIS method in a frequency range of 0.01-105 Hz. The resistance values for GSB, GO, RGO-0.5, RGO-2, and RGO-4 are 1.97, 1.95, 1.80, 1.66, and 1.81 ohm, respectively. The RGO-2 exhibits the lowest resistance among all samples, making it the most conductive and suitable as a supercapacitor electrode. The stability of the samples has been analyzed by measuring C_{SP} from the 1st to the 1000th cycle, as depicted in Figure 12 (b). All samples show very stable C_{SP} up to the 1000th cycle, with C_{SP} values for GSB, GO, RGO-0.5, RGO-2, and RGO-4 as 8.5 F g^{-1}, 33.5 F g^{-1}, 35.5 F g^{-1}, 36 F g^{-1}, and 2.5 F g^{-1}, respectively.
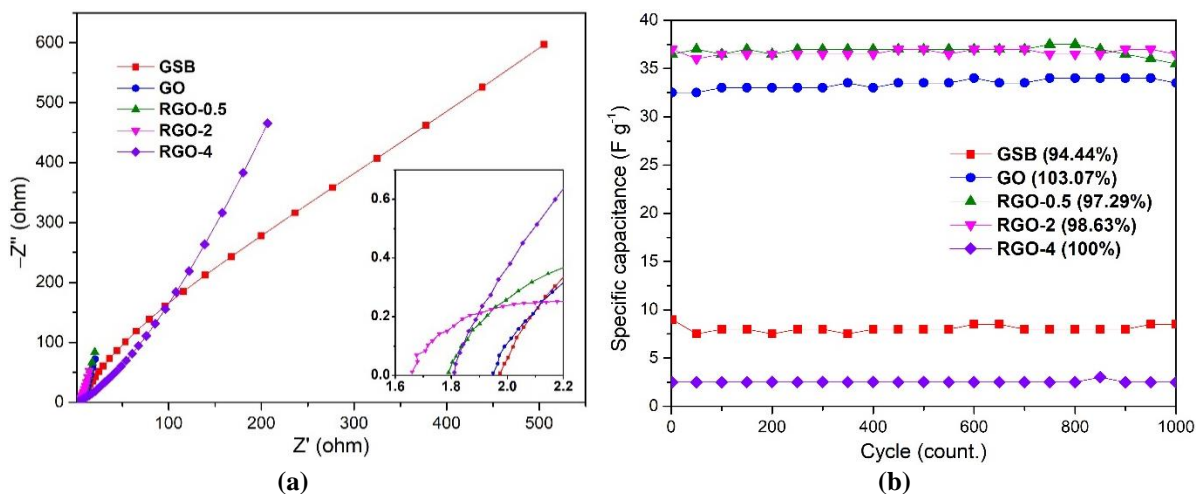

Figure 12. (a) Nyquist plots; **(b)** Retention charge-discharge (RCD).

RGO-2 demonstrates the highest C_{SP} among the samples, with a coulombic efficiency of 98.63%. Therefore, from all electrochemical measurements, RGO-2 exhibits the best performance for supercapacitors in terms of specific capacitance, conductivity, and stability.

4. Conclusions

In conclusion, this study successfully demonstrated the synthesis of reduced graphene oxide (RGO) from sugarcane bagasse (SB) using Hummer's method. The process began with preparing SB, an abundant agricultural waste, which involved drying, mashing, and sieving. Subsequently, SB was pyrolyzed at 750°C under an argon atmosphere to obtain graphite (GSB). Through the Hummer's method, GSB underwent a series of processes, ultimately yielding graphene oxide (GO) products. Further treatment included ultrasonication to break oxygen-functional groups, followed by reduction to RGO using varying amounts of Zn (0.5, 2, and 4 g). The comprehensive characterization techniques employed in this study confirmed the successful synthesis of GO and RGO products. However, it was observed that the concentration of Zn played a critical role in RGO production. Inadequate Zn failed to achieve a complete reduction of GO, while excessive Zn led to the presence of Zn residues in the RGO samples. Therefore, optimizing the Zn concentration is essential to obtaining the desired RGO product. In addition, the electrochemical properties of the synthesized RGO were investigated. The addition of 2 g of Zn (RGO-2) resulted in the best electrochemical performance in specific capacitance, conductivity, and stability, making it a promising electrode material. The methods presented in this work offer a straightforward and effective approach for converting agricultural waste, such as sugarcane bagasse, into value-added products like RGO for supercapacitor applications.

Funding

Conflicts of Interest

The authors declare no conflict of interest.

References

1. Kumar, R.; Naqvi, S.; Gupta, N.; Gaurav, K.; Khan, S.; Kumar, P.; Rana, A.; Singh, R.K.; Bharadwaj, R.; Chand, S. Bulk synthesis of highly conducting graphene oxide with long range ordering. *RSC Adv.* **2015**, *5*, 35893–35898, https://doi.org/10.1039/C5RA01943E.
2. Mbayachi, V.B.; Ndayiragije, E.; Sammani, T.; Taj, S.; Mbuta, E.R.; khan, A.u. Graphene synthesis, characterization and its applications: A review. *Results Chem.* **2021**, *3*, 100163, https://doi.org/10.1016/j.rechem.2021.100163.
3. Magne, T.M.; de Oliveira Vieira, T.; Alencar, L.M.R.; Junior, F.F.M.; Gemini-Piperni, S.; Carneiro, S.V.; Fechine, L.M.U.D.; Freire, R.M.; Golokhvast, K.; Metrangolo, P.; Fechine, P.B.A.; Santos-Oliveira, R. Graphene and its derivatives: understanding the main chemical and medicinal chemistry roles for biomedical applications. *J. Nanostruct. Chem.* **2022**, *12*, 693-727, https://doi.org/10.1007/s40097-021-00444-3.
4. Johns, J.E.; Hersam, M.C. Atomic Covalent Functionalization of Graphene. *Acc. Chem. Res.* **2013**, *46*, 77–86, https://doi.org/10.1021/ar300143e.
5. Cao, Z.; Wen, X.; Quintano, V.; Joshi, R. On the role of functionalization in graphene-moisture interaction. *Curr. Opin. Solid State Mater. Sci.* **2023**, *27*, 101122, https://doi.org/10.1016/j.cossms.2023.101122.

6. Okhay, O.; Tkach, A. Impact of Graphene or Reduced Graphene Oxide on Performance of Thermoelectric Composites. *C* **2021**, *7*, 37, https://doi.org/10.3390/c7020037.

7. Inchingolo, A.M.; Malcangi, G.; Inchingolo, A.D.; Mancini, A.; Palmieri, G.; Di Pede, C.; Piras, F.; Inchingolo, F.; Dipalma, G.; Patano, A. Potential of Graphene-Functionalized Titanium Surfaces for Dental Implantology: Systematic Review. *Coatings* **2023**, *13*, 725, https://doi.org/10.3390/coatings13040725.

8. Sahu, D.; Sutar, H.; Senapati, P.; Murmu, R.; Roy, D. Graphene, Graphene-Derivatives and Composites: Fundamentals, Synthesis Approaches to Applications *J. Compos. Sci.* **2021**, *5*, 181, https://doi.org/10.3390/jcs5070181.

9. Malik, M.T.U.; Sarker, A.; Mahmud Rahat, S.M.S.; Shuchi, S.B. Performance enhancement of graphene/GO/rGO based supercapacitors: A comparative review. *Mater. Today Commun*. **2021**, *28*, 102685, https://doi.org/10.1016/j.mtcomm.2021.102685.

10. Qi, G.; Wang, Q.; Zhang, R.; Guo, Z.; Zhan, D.; Liu, S. Effect of rGO/GNP on the electrical conductivity and piezoresistance of cement-based composite subjected to dynamic loading. *Constr. Build. Mater.* **2023**, *368*, 130340, https://doi.org/10.1016/j.conbuildmat.2023.130340.

11. Thiruppathi, A.R.; van der Zalm, J.; Zeng, L.; Salverda, M.; Wood, P.C.; Chen, A. Effective microwave-hydrothermal reduction of graphene oxide for efficient energy storage. *J. Energy Storage* **2022**, *48*, 103962, https://doi.org/10.1016/j.est.2022.103962.

12. Kumbar, S.S.; Jarali, C.; Talange, D.B.; Kumbar, R.B. Synthesis, comparison and analysis of graphene. *Mater. Today Proc.* **2020**, *26*, 763–765, https://doi.org/10.1016/j.matpr.2019.12.414.

13. Tseng, I.-H.; You, B.-J.; Chang, P.-Y. Sugarcane bagasse supported graphitic carbon nitride for photocatalytic conversion of carbon dioxide. *Catal. Commun.* **2022**, *164*, 106431, https://doi.org/10.1016/j.catcom.2022.106431.

14. Hummers Jr., W.S.; Offeman, R.E. Preparation of Graphitic Oxide. *J. Am. Chem. Soc.* **1958**, *80*, 1339, https://doi.org/10.1021/ja01539a017.

15. Le, G.T.T.; Chanlek, N.; Manyam, J.; Opaprakasit, P.; Grisdanurak, N.; Sreearunothai, P. Insight into the ultrasonication of graphene oxide with strong changes in its properties and performance for adsorption applications. *Chem. Eng. J.* **2019**, *373*, 1212–1222, https://doi.org/10.1016/j.cej.2019.05.108.

16. Zhu, Z.; Zhu, W.; Yi, J.; Liu, N.; Cao, Y.; Lu, J.; Decker, E.A.; McClements, D.J. Effects of sonication on the physicochemical and functional properties of walnut protein isolate. *Food Res. Int.* **2018**, *106*, 853–861, https://doi.org/10.1016/j.foodres.2018.01.060.

17. Yang, J.; Puchberger, M.; Qian, R.; Maurer, C.; Schubert, U. Zinc(II) Complexes with Dangling Functional Organic Groups. *Eur. J. Inorg. Chem.* **2012**, *2012*, 4294–4300, https://doi.org/10.1002/ejic.201200558.

18. Sodeinde, K.O.; Olusanya, S.O.; Lawal, O.S.; Sriariyanun, M.; Adediran, A.A. Enhanced adsorptional-photocatalytic degradation of chloramphenicol by reduced graphene oxide-zinc oxide nanocomposite. *Sci. Rep.* **2022**, *12*, 17054, https://doi.org/10.1038/s41598-022-21266-5.

19. Qiao, L.; Zeng, Y.; Qu, C.Q.; Zhang, H.Z.; Hu, X.Y.; Song, L.J.; Bi, D.M.; Liu, S.J. Adsorption of oxygen atom on Zn-terminated (0001) surface of wurtzite ZnO: A density-functional theory investigation. *Phys. E Low-Dimens. Syst. Nanostructures* **2013**, *48*, 7–12, https://doi.org/10.1016/j.physe.2012.11.020.

20. Sarkar, S.; Basak, D. The reduction of graphene oxide by zinc powder to produce a zinc oxide-reduced graphene oxide hybrid and its superior photocatalytic activity. *Chem. Phys. Lett.* **2013**, *561–562*, 125–130, https://doi.org/10.1016/j.cplett.2013.01.050.

21. Perumal, D.; Albert, E.L.; Abdullah, C.A.C. Green Reduction of Graphene Oxide Involving Extracts of Plants from Different Taxonomy Groups. *J. Compos. Sci.* **2022**, *6*, 58, https://doi.org/10.3390/jcs6020058.

22. Suresh, D.; Udayabhanu; Pavan Kumar, M.A.; Nagabhushana, H.; Sharma, S.C. Cinnamon supported facile green reduction of graphene oxide, its dye elimination and antioxidant activities. *Mater. Lett.* **2015**, *151*, 93–95, https://doi.org/10.1016/j.matlet.2015.03.035.

23. Sadhukhan, S.; Ghosh, T.K.; Rana, D.; Roy, I.; Bhattacharyya, A.; Sarkar, G.; Chakraborty, M.; Chattopadhyay, D. Studies on synthesis of reduced graphene oxide (RGO) via green route and its electrical property. *Mater. Res. Bull.* **2016**, *79*, 41–51, https://doi.org/10.1016/j.materresbull.2016.02.039.

24. Haghighi, B.; Tabrizi, M.A. Green-synthesis of reduced graphene oxide nanosheets using rose water and a survey on their characteristics and applications. *RSC Adv.* **2013**, *3*, 13365–13371, https://doi.org/10.1039/c3ra40856f.

25. Kusrini, E.; Suhrowati, A.; Usman, A.; Degirmenci, V.; Khalil, M. Synthesis and Characterization of Graphite Oxide, Graphene Oxide, and Reduced Graphene Oxide from Graphite Waste Using Modified Hummers' Method and Zinc as Reducing Agent. *Int. J. Technol.* **2019**, *10*, 1093–1104,

https://doi.org/10.14716/ijtech.v10i6.3639.

26. Wannasen, L.; Chanlek, N.; Siriroj, S.; Maensiri, S.; Swatsitang, E.; Pinitsoontorn, S. Enhanced Electrochemical Performance of Sugarcane Bagasse-Derived Activated Carbon via a High-Energy Ball Milling Treatment. *Nanomaterials* **2022**, *12*, 3555, https://doi.org/10.3390/nano12203555.

27. Chen, X.; Qu, Z.; Liu, Z.; Ren, G. Mechanism of Oxidization of Graphite to Graphene Oxide by the Hummers Method. *ACS Omega* **2022**, *7*, 23503–23510, https://doi.org/10.1021/acsomega.2c01963.

28. Maher, M.; Hassan, S.; Shoueir, K.; Yousif, B.; Abo-Elsoud, M.E.A. Activated carbon electrode with promising specific capacitance based on potassium bromide redox additive electrolyte for supercapacitor application. *J. Mater. Res. Technol.* **2021**, *11*, 1232–1244, https://doi.org/10.1016/j.jmrt.2021.01.080.

29. Mishra, N.K.; Mondal, R.; Maiyalagan, T.; Singh, P. Synthesis, Characterizations, and Electrochemical Performances of Highly Porous, Anhydrous $Co_{0.5}Ni_{0.5}C_2O_4$ for Pseudocapacitive Energy Storage Applications. *ACS Omega* **2022**, *7*, 1975–1987, https://doi.org/10.1021/acsomega.1c05356.

30. Cui, L.; Wei, X.; Li, J.; Chang, G.; Huang, X.; Han, D. Structure and Saccharification of Sugarcane Bagasse Pretreated with Acid Coupled Alkaline. In Proceedings of the International Symposium on Mechanical Engineering and Material Science (ISMEMS 2017), Advances in Engineering Research; Publisher, Atlantis Press, **2017**; 104-107, https://doi.org/10.2991/ismems-17.2018.25.

31. Kumar, A.; Singh Negi, Y.; Choudhary, V.; Kant Bhardwaj, N. Characterization of Cellulose Nanocrystals Produced by Acid-Hydrolysis from Sugarcane Bagasse as Agro-Waste. *J. Mater. Phys. Chem.* **2014**, *2*, 1–8, https://doi.org/10.12691/jmpc-2-1-1.

32. Thiangtham, S.; Runt, J.; Saito, N.; Manuspiya, H. Fabrication of biocomposite membrane with microcrystalline cellulose (MCC) extracted from sugarcane bagasse by phase inversion method. *Cellulose* **2020**, *27*, 1367–1384, https://doi.org/10.1007/s10570-019-02866-3.

33. Rajan, A.S.; Sampath, S.; Shukla, A.K. An *in situ* carbon-grafted alkaline iron electrode for iron-based accumulators. *Energy Environ. Sci.* **2014**, *7*, 1110–1116, https://doi.org/10.1039/c3ee42783h.

34. Xu, Y.; Tan, R.; Wu, J.; Huang, J. High-performance supercapacitors based on amorphous carbon derived from natural *Ramulus mori*. *Mater. Adv.* **2022**, *3*, 6878–6886, https://doi.org/10.1039/D2MA00426G.

35. Penki, T.R.; Kishore, B.; Munichandraiah, N.; Shanmughasundaram, D. High Rate Capability of Coconut Kernel Derived Carbon As An Anode Material For Lithium-ion Batteries. *Adv. Mater. Lett.* **2014**, *5*, 184–190, https://doi.org/10.5185/amlett.2013.8530.

36. Hidayah, N.M.S.; Liu, W.-W.; Lai, C.-W.; Noriman, N.Z.; Khe, C.-S.; Hashim, U.; Lee, H.C. Comparison on graphite, graphene oxide and reduced graphene oxide: Synthesis and characterization. *AIP Conf. Proc.* **2017**, *1892*, 150002, https://doi.org/10.1063/1.5005764.

37. Khan, S.A.; Khan, S.B.; Khan, L.U.; Farooq, A.; Akhtar, K.; Asiri, A.M. Fourier Transform Infrared Spectroscopy: Fundamentals and Application in Functional Groups and Nanomaterials Characterization. In Handbook of Materials Characterization, Sharma, S.K., Ed.; Springer International Publishing, Cham, **2018**; 317–344, https://doi.org/10.1007/978-3-319-92955-2_9.

38. Nandiyanto, A.B.D.; Oktiani, R.; Ragadhita, R. HOW TO READ AND INTERPRET FTIR SPECTROSCOPE OF ORGANIC MATERIAL. *Indones. J. Sci. Technol.* **2019**, *4*, 97–118, https://doi.org/10.17509/ijost.v4i1.15806.

39. Ferrari, A.C. Raman spectroscopy of graphene and graphite: Disorder, electron–phonon coupling, doping and nonadiabatic effects. *Solid State Commun.* **2007**, *143*, 47–57, https://doi.org/10.1016/j.ssc.2007.03.052.

40. Malard, L.M.; Pimenta, M.A.; Dresselhaus, G.; Dresselhaus, M.S. Raman spectroscopy in graphene. *Phys. Rep.* **2009**, *473*, 51–87, https://doi.org/10.1016/j.physrep.2009.02.003.

41. Silva, C.; Simon, F.; Friedel, P.; Pötschke, P.; Zimmerer, C. Elucidating the Chemistry behind the Reduction of Graphene Oxide Using a Green Approach with Polydopamine. *Nanomaterials* **2019**, *9*, 902, https://doi.org/10.3390/nano9060902.

42. Papageorgiou, D.G.; Kinloch, I.A.; Young, R.J. Mechanical properties of graphene and graphene-based nanocomposites. *Prog. Mater. Sci.* **2017**, *90*, 75–127, https://doi.org/10.1016/j.pmatsci.2017.07.004.

43. Lee, A.Y.; Yang, K.; Anh, N.D.; Park, C.; Lee, S.M.; Lee, T.G.; Jeong, M.S. Raman study of D* band in graphene oxide and its correlation with reduction. *Appl. Surf. Sci.* **2021**, *536*, 147990, https://doi.org/10.1016/j.apsusc.2020.147990.